Moiré-Modulated Conductance of Hexagonal Boron Nitride Tunnel Barriers

Alex Summerfield[1], Aleksey Kozikov[2,3], Tin S. Cheng[1], Andrew Davies[1,4], Yong-Jin Cho[1], Andrei N. Khlobystov[4,5], Christopher J. Mellor[1], C. Thomas Foxon[1], Kenji Watanabe[6], Takashi Taniguchi[6], Laurence Eaves[1], Kostya S. Novoselov[2,3], Sergei V. Novikov[1] and Peter H. Beton[1].

[1]School of Physics and Astronomy, University of Nottingham, Nottingham, NG7 2RD, UK

[2]School of Physics and Astronomy, University of Manchester, Oxford Road, Manchester, M13 9PL, UK

[3]National Graphene Institute, University of Manchester, Oxford Road, Manchester, M13 9PL, UK

[4]School of Chemistry, University of Nottingham, Nottingham, NG7 2RD, UK

[5]Nottingham Nanoscale and Microscale Research Centre, University of Nottingham, NG7 2RD, UK

[6]The National Institute for Materials Science, Advanced Materials Laboratory, 1-1 Namiki, Tsukuba, Ibraki 305-0044, Japan.

Monolayer hexagonal boron nitride (hBN) tunnel barriers investigated using conductive atomic force microscopy reveal moiré patterns in the spatial maps of their tunnel conductance consistent with the formation of a moiré superlattice between the hBN and an underlying highly ordered pyrolytic graphite (HOPG) substrate. This variation is attributed to a periodic modulation of the local density of states and occurs for both exfoliated hBN barriers and epitaxially-grown layers. The epitaxial barriers also exhibit enhanced conductance at localised sub-nanometre regions which are attributed to exposure of the substrate to a nitrogen plasma source during the high temperature growth process. Our results show clearly a spatial periodicity of tunnel current due to the formation of a moiré superlattice and we argue that this can provide a mechanism for elastic scattering of charge carriers for similar interfaces embedded in graphene/hBN resonant tunnel diodes.

Keywords: boron nitride; epitaxy, growth, tunnelling, superlattice, moiré, heterostructure

*Corresponding author: alex.summerfield@nottingham.ac.uk

Hexagonal boron nitride (hBN) has emerged as one of the most widely investigated [1] 2D materials (2DMs) since the initial isolation of graphene [2]. It is an insulator with a large energy gap of ~6 eV and is isostructural with graphene with a lattice mismatch of only ~1.8% between the two crystals [1]. Heterostructures based on the two crystals represent a new class of functional electronic materials [3–9]. For example, graphene mounted on the atomically flat surface of hBN has a much higher carrier mobility due to the reduction of potential fluctuations encountered in early graphene devices fabricated on SiO_2 [1,10–12]. When the crystal lattice of graphene is overlaid on hBN, an additional physical property emerges, namely the formation of a hexagonal moiré fringe pattern with an associated superlattice potential which leads to pronounced changes in the in-plane magnetoconductivity of graphene through the formation of mini-bands and small energy gaps [3,5,8,13–18]. Moiré patterns might also be expected when hBN layers are placed or grown on graphene/graphite. However, there have been very few reports of the formation of such structures [19–21] although these interfaces form an integral part of graphene/hBN resonant tunnelling diodes and related van der Waals heterostructures [4,19,22–24]. In particular, hBN tunnel barriers have been exploited to produce resonant tunnelling transistors with gate-controlled negative differential conductance [22,25–29].

In this paper we investigate the influence of the formation of a moiré pattern on the tunnelling conductance of a hBN barrier. Using conductive atomic force microscopy (cAFM) we show that there is a pronounced spatial variation in the tunnel current which we attribute to the moiré pattern formed at an hBN/graphite interface. The effect is observed both in heterostructures formed by placement of exfoliated hBN, similar to the process used in the fabrication of most resonant tunnelling diodes [30–33], and also in the interface formed between epitaxially-grown hBN layers and a graphite substrate.

The hBN/graphite tunnel barrier devices investigated here were fabricated using the 'dry-transfer' method [34], and also from hBN grown epitaxially on highly oriented pyrolytic graphite (HOPG) using plasma-assisted molecular beam epitaxy (PA-MBE) following protocols which we have recently reported [19–21]. Samples were then imaged using a combination of AFM/cAFM and scanning tunnelling microscopy (STM) in ambient conditions. The details of the fabrication and imaging procedures for these devices are presented in the supplementary information (SI).

Figure 1a shows a schematic diagram of the exfoliated hBN device. The hBN flake is placed on an exfoliated (multilayer) HOPG layer mounted on a Si/SiO_2 wafer (oxide thickness 300 nm). A thermally evaporated Cr/Au contact is deposited on the HOPG and acts as a counter-electrode to the cAFM tip. An optical micrograph of the HOPG flake and Cr/Au electrode structure is shown in Fig. 1b. The top surface of the flake is covered in exfoliated hBN flakes which cannot be resolved in bright-field optical microscopy, so dark-field optical microscopy is used to highlight the edges of the flakes (see SI Fig. S1b). A monolayer-thick (ML) hBN flake (see Fig. 1c) was selected by performing large area tapping-mode (AC-mode) AFM scans to identify thin flakes. The thickness of the hBN flake, as shown in Fig. 1d, was 0.35 ± 0.05 nm, close to the expected value for 1 ML of hBN.

Figure 2 presents cAFM data acquired on the exfoliated device shown in Fig. 1; the applied voltage between tip and substrate is 10 mV. Figs. 2a and b show simultaneously-acquired contact-mode topography (Fig. 2a) and current channel (Fig. 2b) images of the same region on the ML hBN flake. The surface has a low roughness as indicated by the red line profile in Fig. 2c with no distinct features such as step edges/gaps on the hBN surface; any residual surface roughness is likely due to the underlying SiO_2 support substrate. However, the tunnel current image (Fig. 2b) clearly shows an 11.7 ± 0.1 nm period moiré pattern which is detectable over the entire surface of the hBN flake, indicative of a single crystalline domain. Using a simple geometric relationship[3] and assuming that the hBN is unstrained, we calculate a rotational mismatch of 0.66 ± 0.02° between the HOPG and hBN lattices from the measured moiré periodicity with an expected moiré twist angle of 27.5°

relative to the graphite lattice. We have separately confirmed that the hBN and HOPG lattices are aligned by performing high-speed contact-mode imaging on the hBN flake and HOPG surface near the hBN flake (see Fig. S4b and c). Measurement of the twist angle of the moiré pattern relative to the HOPG lattice (27 ± 1°) also agrees with the expected angle calculated above (Fig. S4d). The formation of the moiré pattern results in a periodic decrease of ~50 % from the peak value of tunnel current along the principal axis of the hexagonal moiré pattern, as shown by the blue line profile in Fig. 2c, with no correlation with the height profile in Fig. 2a. Figure 2d also shows atomic lattice imaging of the hBN surface (acquired in contact mode using high speed scanning, see SI) which confirm the expected lattice spacing of 0.25 ± 0.01 nm for hBN [35].

A schematic of the PA-MBE hBN tunnel barriers is shown in Fig. 3a. As with the exfoliated device, the bulk HOPG substrate provides a counter electrode to the cAFM tip and is electrically connected using conducting silver paint. Following growth (see SI), the HOPG surface is almost completely covered in monolayer-thick hBN (and some regions of bilayer (BL) and multilayer hBN around HOPG step-edges). Optically, the sample has a uniform contrast when observed using bright field microscopy and no surface detail due to the growth is observed (see Fig. S1a). The contact-mode AFM image of the surface topography of the PA-MBE hBN in Fig. 3b shows the laterally polycrystalline ML hBN domains for a sample with a high surface coverage. The expected ~0.35 nm step height of ML hBN is observed in measurements at the edge between ML hBN and uncovered HOPG (see Fig. 3c), in agreement with our previous AFM measurements of MBE-grown hBN on HOPG [19,20].

Figure 4 presents cAFM data for the device with PA-MBE-grown hBN on HOPG. Figure 4a shows the topography of a region consisting of several hBN domains. The central region with darker contrast (i.e. topographically lower) is the HOPG substrate (labelled) which has remained uncovered by hBN growth. Figure 4b shows a cAFM image for the top half of the region in Fig. 4a. The line profiles along this central region (blue and red lines in Figs. 4a and b) are plotted in the inset of Fig. 4a where exposed HOPG is present indicates that the uncovered HOPG has significantly higher tip-sample

junction conductance, as expected. Also indicated in both Figs. 4a and b are the positions where images Fig. 4 c and e were acquired. High-resolution images of the hBN domains are shown in Figs. 4c and e. In some domains, we observe moiré patterns in the tunnel conductance signal. An example is shown in Fig. 4c in which a spatial variation of tunnel current with a period of 13.5 ± 0.1 nm is observed, indicating a small rotational mismatch of 0.25 ± 0.04° between the hBN and HOPG lattices [3]. A line-profile across the moiré pattern along this feature (Fig. 4d) shows a ~50 % decrease in the tunnel current from the maximum value along the moiré fringes, similar to the variation observed in the measurements of the exfoliated hBN device. In addition to the periodic variation, some localised regions of higher surface conductance are observed which are discussed later.

In addition, Figure 4e shows one hBN domain in which no moiré pattern is resolved. This suggests that any moiré pattern present has either a period or amplitude which is too small to resolve, possibly due to the misalignment of hBN and underlying HOPG. The current spikes in the conductance profile and bright features in the cAFM current maps (Fig. 4c-e) are consistent across several scans and are observed both on hBN domains that show moiré fringes and also those on which no moiré pattern is resolved, indicating localised regions of high surface conductance. Analysis of the increase in conductance at these spots (See Fig. S2) shows a typical 2 to 3-fold increase relative to the average conductance of the whole cAFM image for the regions shown in Figs. 4c and e respectively, with some regions showing increases as high as a factor of ~13.

High resolution lattice imaging (and simultaneous acquisition of tunnel current signal; Fig. 4g and h) of the hBN lattice around these regions of high conductance yield the periodicity of the hBN lattice (0.25 ± 0.01 nm) as is the case for the exfoliated device shown in Fig. 2. This allows us to image the individual regions of high conductance and shows that they are localised around an area of approximately one lattice site, although we do not observe any lattice vacancies or defects in contact mode images of the hBN layer in this region (Fig. 4g). As no vacancy is observed in the lattice of the PA-MBE hBN layer using topographic imaging, we speculate that the highly conducting regions

observed in our MBE hBN samples may be caused by defects in the underlying HOPG substrate, introduced, for example, by exposure of the HOPG substrate to a N_2 plasma during the growth process [36]. In order to test this hypothesis, we imaged the regions of HOPG not covered by hBN growth with cAFM. A current map of a region of exposed HOPG is shown in Fig. 4f and reveals a non-uniform current density profile, similar to the region in Fig. 4e with ML hBN coverage. For these regions, however, we were unable to achieve lattice-level resolution in both height and current-channels. To further investigate the effect of N_2 plasma on the HOPG surface, we subjected clean HOPG substrates to the same high-temperature conditions used to grow the PA-MBE sample shown in Figs. 3 and 4, both with and without the presence of an N_2 plasma. cAFM images of these samples (Fig. S3a and d) show clearly that defects are formed on the surface through exposure to the N_2 plasma rather than high temperature annealing alone.

Since the formation of a moiré superlattice between hBN and graphite modifies the local density of states (LDOS) of the hBN layer, we performed ambient STM imaging in order to confirm our cAFM observations. STM can typically provide better contrast than cAFM as it is highly sensitive to variations in surface LDOS and has potentially higher lateral resolution than AFM in ambient conditions. Figure 5 presents constant-current STM images of the PA-MBE hBN surface. As expected, large-area STM images of the PA-MBE hBN surface show that multiple domains of ML hBN and some regions of BL hBN are present; these are shown in Fig. 5a. Several different surface features appear in the main image which confirm the laterally polycrystalline nature of the grown hBN layers; these are revealed in more detail in the further sub-figures. In addition, the STM images show that a range of moiré periodicities are present, confirming that there are multiple rotational alignments with the substrate [3,10]. Figure 5b shows two neighbouring hBN domains which exhibit moiré patterns of differing rotational alignment with the underlying HOPG, the left domain having a moiré period of ~16 nm and the right domain of ~14 nm, indicating that both of these domains are closely aligned with the HOPG lattice. Interestingly, the larger moiré period (~16 nm) region has a periodicity greater than the maximum moiré period expected for aligned HBN and HOPG lattices (~14 nm). This

indicates that the hBN lattice is compressively strained by ~0.24 % in this region, assuming that the hBN and graphite lattices are perfectly aligned [13,14,37–39].

Figure 5c and associated line profiles in Fig. 5j confirm the presence of the small, high-conductance regions on the hBN surface in our STM images. This supports our cAFM observations in Fig. 4. Figure 5d-i show images of both ML and BL regions of hBN that have a common rotational alignment. Figure 5d shows a BL hBN island (darker contrast due to reduced tunnel conduction through the thicker hBN) surrounded by ML hBN. High resolution imaging of both the ML and BL islands (Fig. 5e & g) show that both regions exhibit aligned, short-period moiré patterns with a periodicity of 2.4 ± 0.01 nm, suggesting that the BL region is growing epitaxially on the ML hBN with a common misalignment of 5.8 ± 0.3° to the underlying HOPG[3]. Further imaging of another epitaxial BL region neighbouring the ML region in Fig. 5d is shown in Fig. 5i, this area also exhibits a moiré pattern aligned with the ML region with the same 2.4 nm moiré periodicity, indicating that they also share a common rotational alignment with the HOPG substrate. It is possible that these regions with smaller moiré periods correspond to areas where no moiré is resolved in cAFM images.

Our measurements reveal the presence of local electronic moiré effects in hBN tunnel barriers due to rotational misalignment of both exfoliated and PA-MBE-grown hBN on HOPG. The periodic current modulation which we observe in cAFM implies that tunnelling electrons in a hBN/graphene heterostructure experience a variation in potential landscape with a period equal to that of the moiré pattern. It might be anticipated that this periodic variation would provide a source of elastic scattering [40] in which the in-plane wave vector, k, of a tunnelling electron would be scattered by k^i_M (i= 1 ,2), the reciprocal lattice vector of the moiré pattern, and this mechanism may also be relevant to the buried interfaces formed in graphene/hBN resonant tunnelling diodes.

The topographic structure of the two types of hBN tunnel barrier studied here differ significantly from each other. Nevertheless, despite some differences in their microscopic structure, cAFM imaging of ML hBN shows broadly the same tunnel current behaviour, with both samples exhibiting

hexagonal moiré patterns. In addition, for both exfoliated and PA-MBE grown devices, our maps of tunnel current reveal a similar variation in the tunnel current along the principal axes of the moiré pattern. The observation of a moiré pattern with a periodicity larger than expected for aligned hBN on graphite is particularly interesting since it implies that in these areas the lattice mismatch between the hBN and graphite must be reduced which would be consistent with a compressive strain in the epitaxial growth layer.

Our observations of an increased localised conductance in the MBE-grown hBN samples, which we attribute to plasma-induced defects in the HOPG, show that the effects of substrate damage need to be considered in the future fabrication of 2DM vdW heterostructures grown using plasma-assisted methods. We plan to follow up these observations with studies using a combination of low temperature UHV AFM and STM measurements in order to fully characterise the electronic behaviour of these defects. Overall, our results show that moiré effects, which have been demonstrated to lead to pronounced changes in the properties of graphene on hBN, also lead to significant modifications of the electronic properties of the inverse structures, namely hBN on graphene. These differences are present in both the epitaxial and exfoliated devices, thus offering the prospect of high-quality epitaxial materials by growing at high temperatures using PA-MBE. This technique could provide a platform for the growth of hBN/graphene heterostructures in which strain and moiré pattern modulation of electronic properties can be introduced in a controlled way.

ACKNOWLEDGMENTS

This work was supported by the Engineering and Physical Sciences Research Council [Grant numbers EP/L013908/1, EP/P019080/1, DTP grant EP/M50810X/1]; the Leverhulme Trust [Grant number RPG-2014-129]; the EU Graphene Flagship Program; the European Research Council Synergy Grant Hetero2D; The Royal Society and the US Army Research Office (W911NF-16-1-0279), K.W. and T.T.

acknowledge support from the Elemental Strategy Initiative conducted by the MEXT, Japan and the CREST (JPMJCR15F3).

SUPPORTING INFORMATION

Experimental and growth methodologies for both MBE and exfoliated hBN tunnel barriers; optical images of hBN samples; histogram of conductance spikes in MBE hBN devices; cAFM imaging of annealed and N_2 plasma treated HOPG samples.

DATA AVAILABILITY

All data on which this paper is based may be publicly accessed at http://rdmc.nottingham.ac.uk/ under doi.org/10.17639/nott.358.

REFERENCES

(1) Dean, C. R.; Young, A. F.; Meric, I.; Lee, C.; Wang, L.; Sorgenfrei, S.; Watanabe, K.; Taniguchi, T.; Kim, P.; Shepard, K. L.; Hone, J. *Nat. Nanotechnol.* **2010**, *5*, 722–726.

(2) Novoselov, K. S.; Geim, A. K.; Morozov, S. V.; Jiang, D.; Zhang, Y.; Dubonos, S. V.; Grigorieva, I. V.; Firsov, A. A. *Science* **2004**, *306*, 666–669.

(3) Yankowitz, M.; Xue, J.; Cormode, D.; Sanchez-Yamagishi, J. D.; Watanabe, K.; Taniguchi, T.; Jarillo-Herrero, P.; Jacquod, P.; LeRoy, B. J. *Nat. Phys.* **2012**, *8*, 382–386.

(4) Britnell, L.; Gorbachev, R. V.; Jalil, R.; Belle, B. D.; Schedin, F.; Mishchenko, A.; Georgiou, T.; Katsnelson, M. I.; Eaves, L.; Morozov, S. V.; Peres, N. M. R.; Leist, J.; Geim, A. K.; Novoselov, K. S.; Ponomarenko, L. A. *Science* **2012**, *335*, 947–950.

(5) Dean, C. R.; Wang, L.; Maher, P.; Forsythe, C.; Ghahari, F.; Gao, Y.; Katoch, J.; Ishigami, M.; Moon, P.; Koshino, M.; Taniguchi, T.; Watanabe, K.; Shepard, K. L.; Hone, J.; Kim, P. *Nature* **2013**, *497*, 598–602.

(6) Eckmann, A.; Park, J.; Yang, H.; Elias, D.; Mayorov, A. S.; Yu, G.; Jalil, R.; Novoselov, K. S.; Gorbachev, R. V.; Lazzeri, M.; Geim, A. K.; Casiraghi, C. *Nano Lett.* **2013**, *13*, 5242–5246.

(7) Wang, L.; Meric, I.; Huang, P. Y.; Gao, Q.; Gao, Y.; Tran, H.; Taniguchi, T.; Watanabe, K.; Campos, L. M.; Muller, D. A.; Guo, J.; Kim, P.; Hone, J.; Shepard, K. L.; Dean, C. R. *Science* **2013**, *342*, 614–617.

(8) Ponomarenko, L. A.; Gorbachev, R. V; Yu, G. L.; Elias, D. C.; Jalil, R.; Patel, A. A.; Mishchenko, A.; Mayorov, A. S.; Woods, C. R.; Wallbank, J. R.; Mucha-Kruczynski, M.; Piot, B. A.; Potemski, M.; Grigorieva, I. V; Novoselov, K. S.; Guinea, F.; Fal'ko, V. I.; Geim, A. K. *Nature* **2013**, *497*, 594–597.

(9) Mayorov, A. S.; Gorbachev, R. V.; Morozov, S. V.; Britnell, L.; Jalil, R.; Ponomarenko, L. A.; Blake, P.; Novoselov, K. S.; Watanabe, K.; Taniguchi, T.; Geim, A. K. *Nano Lett.* **2011**, *11*, 2396–2399.

(10) Decker, R.; Wang, Y.; Brar, V. W.; Regan, W.; Tsai, H. Z.; Wu, Q.; Gannett, W.; Zettl, A.;

Crommie, M. F. *Nano Lett.* **2011**, *11*, 2291–2295.

(11) Xue, J.; Sanchez-Yamagishi, J.; Bulmash, D.; Jacquod, P.; Deshpande, A.; Watanabe, K.; Taniguchi, T.; Jarillo-Herrero, P.; Leroy, B. J. *Nat. Mater.* **2011**, *10*, 282–285.

(12) Das Sarma, S.; Hwang, E. H. *Phys. Rev. B - Condens. Matter Mater. Phys.* **2011**, *83*, 121405.

(13) Woods, C. R.; Britnell, L.; Eckmann, A.; Ma, R. S.; Lu, J. C.; Guo, H. M.; Lin, X.; Yu, G. L.; Cao, Y.; Gorbachev, R. V; Kretinin, A. V; Park, J.; Ponomarenko, L. A.; Katsnelson, M. I.; Gornostyrev, Y. N.; Watanabe, K.; Taniguchi, T.; Casiraghi, C.; Gao, H.; Geim, A. K.; Novoselov, K. S. *Nat. Phys.* **2014**, *10*, 451–456.

(14) Summerfield, A.; Davies, A.; Cheng, T. S.; Korolkov, V. V.; Cho, Y.; Mellor, C. J.; Foxon, C. T.; Khlobystov, A. N.; Watanabe, K.; Taniguchi, T.; Eaves, L.; Novikov, S. V.; Beton, P. H. *Sci. Rep.* **2016**, *6*, 22440.

(15) Tang, S.; Wang, H.; Zhang, Y.; Li, A.; Xie, H.; Liu, X.; Liu, L.; Li, T.; Huang, F.; Xie, X.; Jiang, M. *Sci. Rep.* **2013**, *3*, 2666.

(16) Hunt, B.; Sanchez-Yamagishi, J. D.; Young, A. F.; Yankowitz, M.; Leroy, B. J.; Watanabe, K.; Taniguchi, T.; Moon, P.; Koshino, M.; Jarillo-Herrero, P.; Ashoori, R. C. *Science* **2013**, *340*, 1427–1431.

(17) Wallbank, J. R.; Mucha-Kruczyński, M.; Chen, X.; Fal'ko, V. I. *Ann. Phys.* **2015**, *527*, 359–376.

(18) Wallbank, J. R.; Patel, A. A.; Mucha-Kruczyński, M.; Geim, A. K.; Fal'Ko, V. I. *Phys. Rev. B - Condens. Matter Mater. Phys.* **2013**, *87*, 245408.

(19) Cho, Y.; Summerfield, A.; Davies, A.; Cheng, T. S.; Smith, E. F.; Mellor, C. J.; Khlobystov, A. N.; Foxon, C. T.; Eaves, L.; Beton, P. H.; Novikov, S. V. *Sci. Rep.* **2016**, *6*, 34474.

(20) Vuong, P.; Cassabois, G.; Valvin, P.; Rousseau, E.; Summerfield, A.; Mellor, C.; Cho, Y.; Cheng, T.; Albar, J. D.; Eaves, L.; Foxon, C.; Beton, P.; Novikov, S.; GIL, B. *2D Mater.* **2017**, *4*, 21023.

(21) Cheng, T. S.; Summerfield, A.; Mellor, C. J.; Davies, A.; Khlobystov, A. N.; Eaves, L.; Foxon, C. T.; Beton, P. H.; Novikov, S. V. *J. Vac. Sci. Technol. B, Nanotechnol. Microelectron. Mater. Process. Meas. Phenom.* **2018**, *36*, 02D103.

(22) Britnell, L.; Gorbachev, R. V; Geim, A. K.; Ponomarenko, L. A.; Mishchenko, A.; Greenaway, M. T.; Fromhold, T. M.; Novoselov, K. S.; Eaves, L. *Nat. Commun.* **2013**, *4*, 1794–1795.

(23) Amet, F.; Williams, J. R.; Garcia, A. G. F.; Yankowitz, M.; Watanabe, K.; Taniguchi, T.; Goldhaber-Gordon, D. *Phys. Rev. B - Condens. Matter Mater. Phys.* **2012**, *85*, 73405.

(24) Britnell, L.; Gorbachev, R. V.; Jalil, R.; Belle, B. D.; Schedin, F.; Katsnelson, M. I.; Eaves, L.; Morozov, S. V.; Mayorov, A. S.; Peres, N. M. R.; Castro Neto, A. H.; Leist, J.; Geim, A. K.; Ponomarenko, L. A.; Novoselov, K. S. *Nano Lett.* **2012**, *12*, 1707–1710.

(25) Vdovin, E. E.; Mishchenko, A.; Greenaway, M. T.; Zhu, M. J.; Ghazaryan, D.; Misra, A.; Cao, Y.; Morozov, S. V.; Makarovsky, O.; Fromhold, T. M.; Patanè, A.; Slotman, G. J.; Katsnelson, M. I.; Geim, A. K.; Novoselov, K. S.; Eaves, L. *Phys. Rev. Lett.* **2016**, *116*, 186603.

(26) Mishchenko, A.; Tu, J. S.; Cao, Y.; Gorbachev, R. V; Wallbank, J. R.; Greenaway, M. T.; Morozov, V. E.; Morozov, S. V; Zhu, M. J.; Wong, S. L.; Withers, F.; Woods, C. R.; Kim, Y.-J.; Watanabe, K.; Taniguchi, T.; Vdovin, E. E.; Makarovsky, O.; Fromhold, T. M.; Fal'ko, V. I.; Geim, A. K.; Eaves, L.; Novoselov, K. S. *Nat. Nanotechnol.* **2014**, *9*, 808–813.

(27) Greenaway, M. T.; Vdovin, E. E.; Mishchenko, A.; Makarovsky, O.; Patane, A.; Wallbank, J. R.; Cao, Y.; Kretinin, A. V; Zhu, M. J.; Morozov, S. V; Fal[rsquor]ko, V. I.; Novoselov, K. S.; Geim, A. K.; Fromhold, T. M.; Eaves, L. *Nat. Phys.* **2015**, *11*, 1057–1062.

(28) Gaskell, J.; Eaves, L.; Novoselov, K. S.; Mishchenko, A.; Geim, A. K.; Fromhold, T. M.; Greenaway, M. T. *Appl. Phys. Lett.* **2015**, *107*, 103105.

(29) Feenstra, R. M.; Jena, D.; Gu, G. *J. Appl. Phys.* **2012**, *111*, 43711.

(30) Pizzocchero, F.; Gammelgaard, L.; Jessen, B. S.; Caridad, J. M.; Wang, L.; Hone, J.; Bøggild, P.; Booth, T. J. *Nat. Commun.* **2016**, *7*, 11894.

(31) Kim, K.; Yankowitz, M.; Fallahazad, B.; Kang, S.; Movva, H. C. P.; Huang, S.; Larentis, S.; Corbet, C. M.; Taniguchi, T.; Watanabe, K.; Banerjee, S. K.; Leroy, B. J.; Tutuc, E. *Nano Lett.* **2016**, *16*, 1989–1995.

(32) Castellanos-Gomez, A.; Buscema, M.; Molenaar, R.; Singh, V.; Janssen, L.; van der Zant, H. S.

J.; Steele, G. A. *2D Mater.* **2014**, *1*, 11002.

(33) Zomer, P. J.; Guimaraes, M. H. D.; Brant, J. C.; Tombros, N.; Van Wees, B. J. *Appl. Phys. Lett.* **2014**, *105*, 13101.

(34) Caldwell, J. D.; Anderson, T. J.; Culbertson, J. C.; Jernigan, G. G.; Hobart, K. D.; Kub, F. J.; Tadjer, M. J.; Tedesco, J. L.; Hite, J. K.; Mastro, M. A.; Myers-Ward, R. L.; Eddy, C. R.; Campbell, P. M.; Gaskill, D. K. *ACS Nano* **2010**, *4*, 1108–1114.

(35) Lynch, R. W.; Drickamer, H. G. *J. Chem. Phys.* **1966**, *44*, 181–184.

(36) Heilmann, M.; Bashouti, M.; Riechert, H.; Lopes, J. M. J. *2D Mater.* **2018**, *5*, 25004.

(37) Tang, S.; Wang, H.; Wang, H. S.; Sun, Q.; Zhang, X.; Cong, C.; Xie, H.; Liu, X.; Zhou, X.; Huang, F.; Chen, X.; Yu, T.; Ding, F.; Xie, X.; Jiang, M. *Nat. Commun.* **2015**, *6*, 6499.

(38) Yang, W.; Chen, G.; Shi, Z.; Liu, C.-C.; Zhang, L.; Xie, G.; Cheng, M.; Wang, D.; Yang, R.; Shi, D.; Watanabe, K.; Taniguchi, T.; Yao, Y.; Zhang, Y.; Zhang, G. *Nat. Mater.* **2013**, *12*, 792–797.

(39) Davies, A.; Albar, J. D.; Summerfield, A.; Thomas, J. C.; Cheng, T. S.; Korolkov, V. V.; Stapleton, E.; Wrigley, J.; Goodey, N. L.; Mellor, C. J.; Khlobystov, A. N.; Watanabe, K.; Taniguchi, T.; Foxon, C. T.; Eaves, L.; Novikov, S. V.; Beton, P. H. *Nano Lett.* **2017**, *18*, 498–504.

(40) Amorim, B.; Ribeiro, R. M.; Peres, N. M. R. *Phys. Rev. B* **2016**, *93*, 235403.

FIGURES

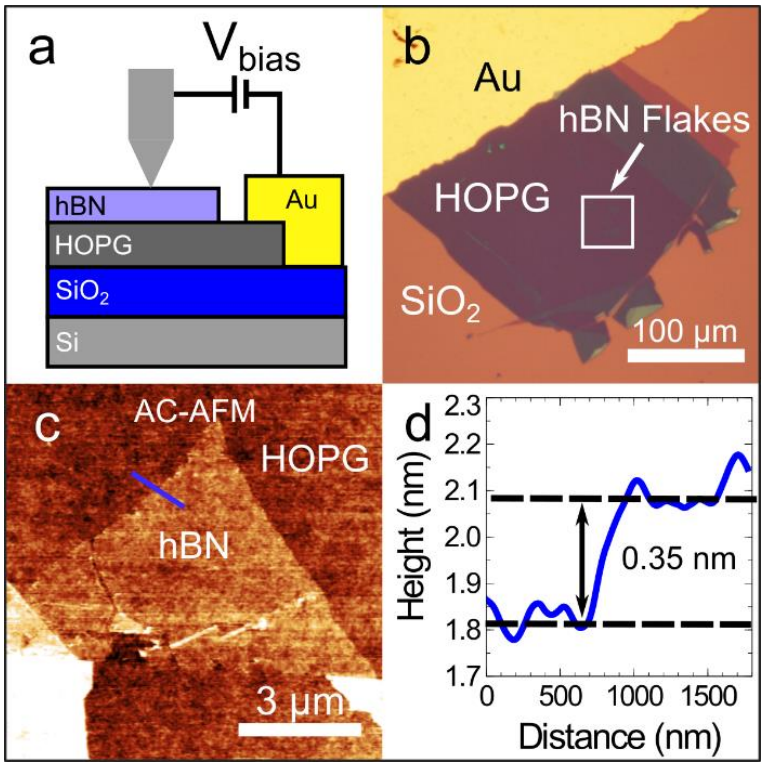

Figure 1. **a**) Schematic of exfoliated hBN/HOPG tunnel barrier device. **b**) Bright-field optical image of the device. The white box indicates the approximate position of the exfoliated hBN flakes. Dark-field optical imaging of this region is given in the supporting information, see Fig. S1. **c**) AC-mode AFM image of part of the region indicated by the white box in image **b,** showing a monolayer hBN flake**. d**) Line profile along the region indicated by the blue line in **c** demonstrating the monolayer thickness of the exfoliated hBN flake.

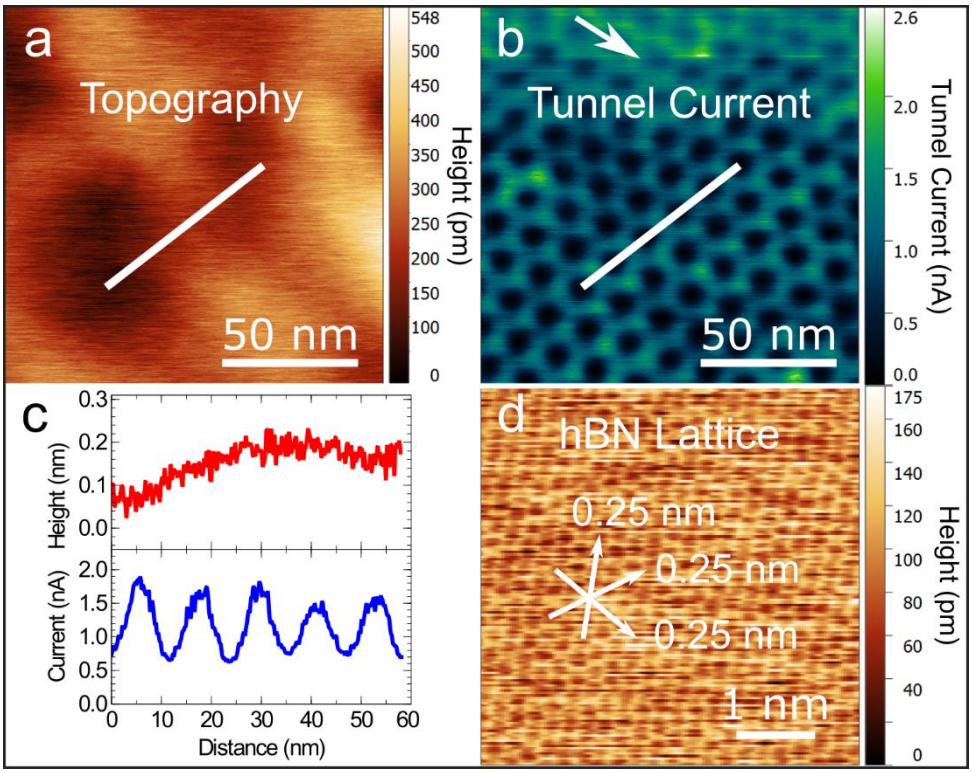

Figure 2. cAFM images of the exfoliated hBN/HOPG device shown in Fig. 1. **a**) Height-channel image of the surface topography of hBN. **b**) Current map of the same area as in image **a,** exhibiting an 11.7 nm moiré pattern due to rotational misalignment between the hBN and HOPG lattices (cAFM tip bias: +10 mV). **c**) (top) Height profile along the line indicated in **a**. (bottom) Conductance profile along the line indicated in **b** showing a spatial variation in tunnel current across the hBN surface (bottom). **d**) Contact mode lattice image showing the hBN lattice and expected hBN periodicity.

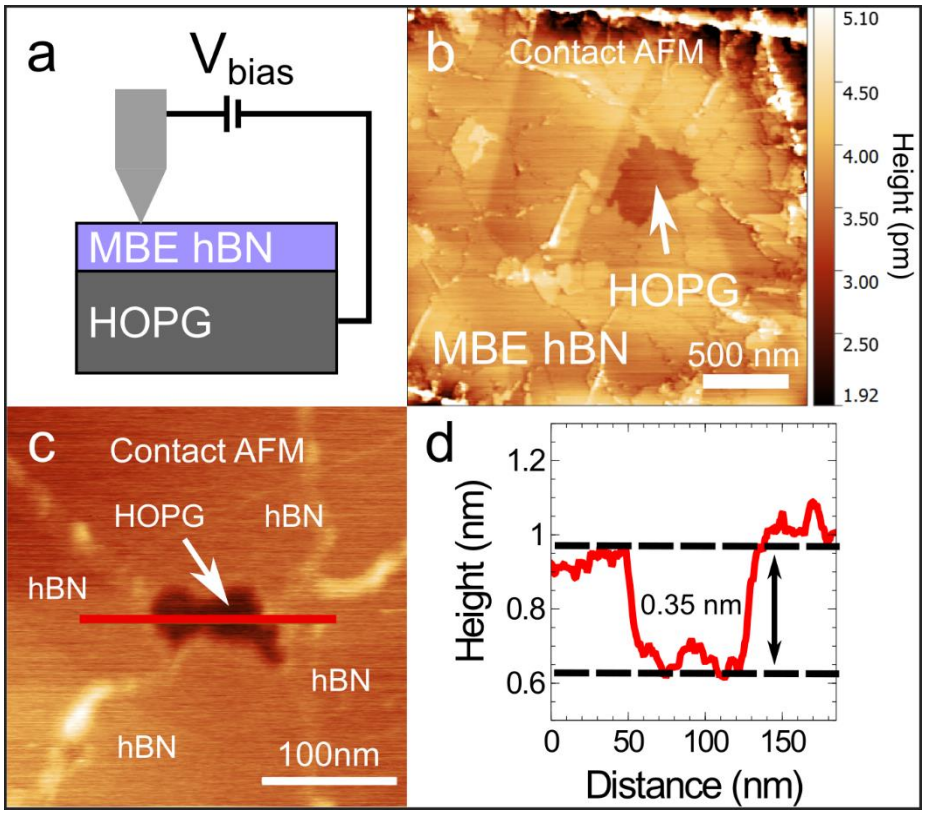

Figure 3. **a**) Schematic of PA-MBE hBN/HOPG device and the experimental setup for cAFM imaging. **b)** Contact mode AFM image of MBE hBN on HOPG; the arrow indicates a region of HOPG not covered by PA-hBN growth. **c**) Contact mode AFM images of multiple hBN domains around a small region of HOPG not covered by hBN growth (dark indicated area). **d**) Height profile along the red line in **c** indicating the monolayer hBN thickness.

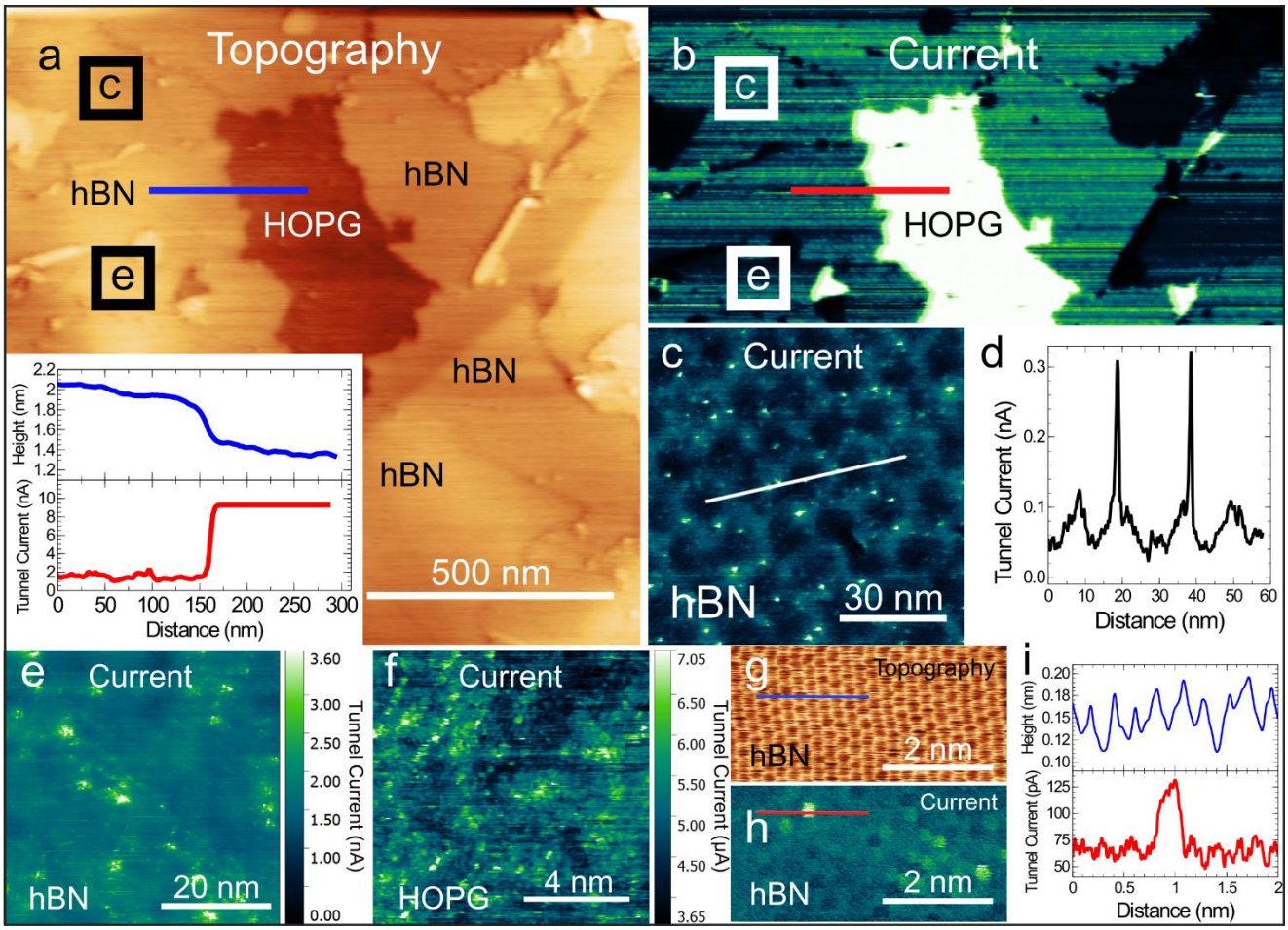

Figure 4. Topographic and cAFM images of PA-MBE grown hBN on HOPG; the label in each image indicates the imaging mode (top label) and/or the surface being imaged (bottom left label). **a**) contact-mode AFM image showing PA-MBE hBN domains with an exposed area of HOPG indicted by the labels. The boxes show the positions of the high-resolution scans of the hBN domains for images **c** and **e**. (**inset**) Line profiles along the regions indicated by the blue and red lines in **a** and **b** respectively at an interface between PA-MBE hBN and exposed HOPG. **b**) Current channel image of the top half of **a**. The labelled boxes correspond to the same regions labelled in **a**, showing where high resolutions scans were taken. **c**) Tunnel current map of the region indicated by the topmost white box in image **b** showing a moiré pattern with a period of 13.5 nm. **d**) Line profile across the white line in image **c** showing the variation in tunnel current. **e**) Tunnel current channel image of non-aligned PA-hBN exhibiting no moiré pattern in the current signal. **f**) Current map of an exposed HOPG region with no hBN overgrowth. **g**) Contact mode AFM image showing the hBN lattice. **h**) Tunnel current channel of **b** showing localised hot-spots of increased conductance. **i**) Height profile (top) and tunnel current profile (bottom) along the blue and red lines marked in **g** and **h** respectively. All cAFM images were taken with a tip bias of +100 mV with the exception of **h** which was acquired using a tip bias of +10 mV.

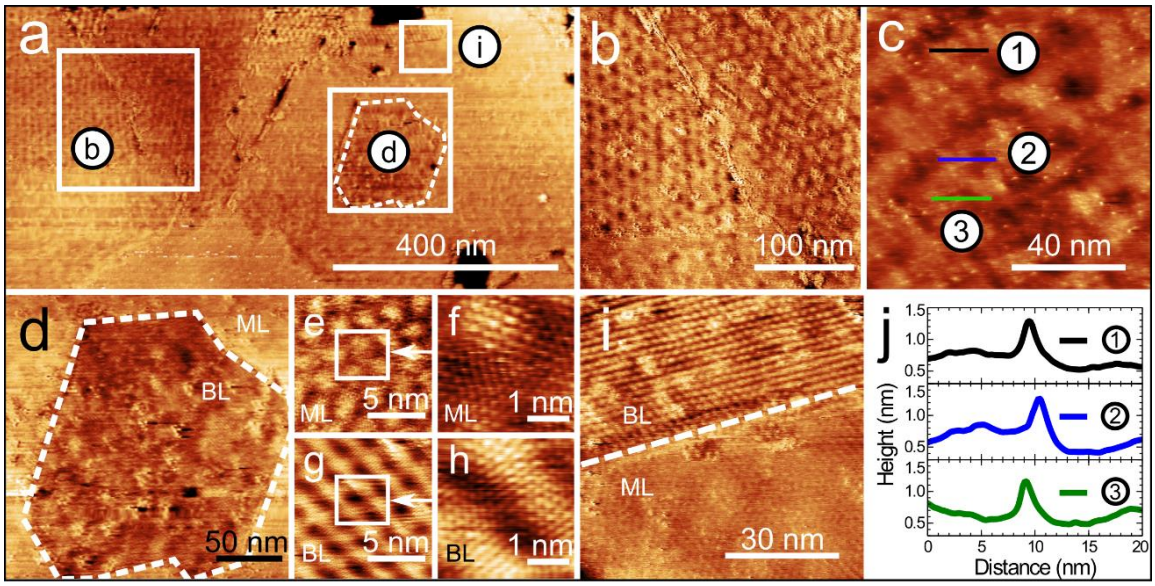

Figure 5. Constant current STM images of hBN grown on HOPG using PA-MBE. **a**) STM image showing multiple domains of hBN grown on HOPG. The white boxes indicate the regions shown in images **b**, **d** and **i** respectively. **b**) Moiré patterns visible on either side of the boundary between two hBN domains, indicated by the white box in **a**. The moiré periods on the left and right domains are 16 nm and 14 nm respectively. **c**) STM image of a monolayer hBN domain on HOPG without moiré patterns showing small regions of increased brightness (i.e. higher STM topography). The profiles indicated by the coloured lines are shown in **j**. **d**) STM image of a bilayer (BL) hBN domain surrounded by monolayer (ML) hBN as indicated by the box in **a**. **e**) Moiré patterns visible on ML hBN region in **d**. **f**) Zoom of **e** showing lattice-level contrast of ML hBN domain. g) STM image of moiré patterns visible on BL hBN domain shown in **d**. **h**) Zoom of **g** showing lattice-level contrast of BL hBN. **i**) STM image showing border between ML and BL hBN as indicated by the white box in **a**. In both regions, moiré patterns are visible and have a periodicity of 2.4 ± 0.1 nm for both the ML and BL regions respectively. **j**) Constant current profiles along the lines indicated in **c** showing small regions with increased tunnel conductance.